Contents list available at CBIORE journal website

International Journal of Renewable Energy Development

Journal homepage: https://ijred.cbiore.id

Research Article

Wind turbine fault estimation using sliding mode observer based on Takagi–Sugeno fuzzy model

Mohammed Taouil[a*], Salaheddine Zouirech[a], Abdelghani El Ougli[b], Belkassem Tidhaf[a]

[a]*Electronics and Systems Laboratory - LES, Faculty of Sciences Oujda, Embeded Systems, Renewable Energy and Artificial Intelligence Team, ENSA, Oujda, Morocco*

[b]*Electronics, Signals, Systems and Computer Science Laboratory (LESSI), Faculty of Science, Sidi Mohamed Ben Abdellah University Fez, Morocco*

Abstract. This paper presents a fault-estimation approach for utility-scale wind turbines that combines Takagi–Sugeno (TS) fuzzy modeling with a sliding-mode observer (SMO). The nonlinear dynamics of the 4.8 MW benchmark turbine are represented by a TS structure, enabling an LMI-based synthesis of a robust TS–SMO. The proposed observer reconstructs both actuator faults affecting generator torque and sensor faults in blade-pitch measurements. MATLAB/Simulink validations under realistic operating conditions (operating-point variations, wind fluctuations, and disturbances) demonstrate accurate tracking and fast, stable fault reconstruction over the complete simulation horizon. Performance is assessed using the Normalized Sum of Squared Errors (NSSE): the reconstructed faults exhibit low NSSE values in the considered fault scenarios, with the blade-pitch sensor fault achieving NSSE =0.087 %. These results indicate reliable fault estimation while maintaining bounded residuals and avoiding drift. The method relies on standard industrial signals and entails modest online computations (matrix operations and a bounded switching term), facilitating integration into existing condition-monitoring and fault-tolerant control architectures. Overall, TS-guided sliding-mode observation is shown to be an effective and robust solution for wind-turbine fault diagnosis under nonlinearities and exogenous perturbations.

Keywords: Actuator faults, Fault diagnosis, Fault reconstruction, LMI, Observer design, Sensor faults, Sliding Mode Observer, Takagi–Sugeno Fuzzy model, Wind energy.

Received: 20th Oct 2025; Revised: 26th Dec 2025; Accepted: 22nd January 2026; Available online: 5th Feb 2026

1. Introduction

Global wind deployment continued to expand in 2024, with about 117 GW of new installations and a cumulative capacity near 1,136 GW by year-end (GWEC, 2025). Across Africa, several markets remain active; Morocco, in particular, maintains its leadership with ~2.4 GW after a ~302 MW addition in 2024 (WWEA, 2025). In this context, ensuring the reliability and availability of wind turbines (WTs) is essential to safeguard energy yield and reduce O&M costs, as undetected faults can compromise safety and cause significant economic losses (GWEC, 2025; WWEA, 2025).

Within wind-turbine fault detection and diagnosis (FDD), two complementary families are widely used: model-based approaches, which exploit physics-informed representations to generate residuals (Dey, Pisu & Ayalew, 2015), and data-driven approaches, which learn fault indicators directly from SCADA and condition-monitoring data (Zhao *et al*., 2018). In practice, both paradigms are often combined to leverage physical insight and statistical patterns in the data (Gao & Liu, 2021; Wu *et al.,* 2021; Zhang *et al*., 2021).

Bridging these strands, operational monitoring requires residuals that are causal, physically interpretable, and selectively sensitive to faults while remaining insensitive to wind turbulence, load variations, and modeling errors; estimation errors should admit computable bounds and gain tuning should expose explicit robustness margins under parameter drift and sensor noise. In practice, this points to observer formulations that embed plant physics and enforce structure, through rank conditions for disturbance decoupling, scheduling over operating regions via LPV or TS models, and convex LMI syntheses, so that residual directionality and fault identifiability are preserved within real-time computation budgets. Robust $\boldsymbol{H}_\infty$ filtering and sliding-mode mechanisms then complement these structures by guaranteeing bounded error dynamics and fast convergence, providing a pragmatic path from residual generation to decision-grade diagnosis in industrial settings (Chen & Patton, 1999; Boyd *et al.,* 1994; Apkarian & Gahinet, 1995; Mazenc & Bernard, 2011; Efimov, Raïssi, Zolghadri & Perruquetti, 2016).

Among model-based FDD strategies for wind turbines, Kalman-filter estimators (extended/unscented variants included) are widely used to monitor sensor and actuator faults in simulation and practice, offering optimal state estimation and noise attenuation but remaining sensitive to model fidelity and covariance tuning (Cao, Chen & Jiang, 2016). Luenberger observers and observer banks generate residuals suitable for threshold-based detection (Dey, Pisu & Ayalew, 2015), while unknown-input observers can decouple unmeasured disturbances under specific structural conditions, albeit at the cost of added design complexity especially when combined with

* Corresponding author
Email: t123med@hotmail.fr (M. Taouil)

https://doi.org/10.61435/ijred.2026.61895
ISSN: 2252-4940/© 2026.The Author(s). Published by CBIORE

robust schemes such as $\boldsymbol{H}_\infty$ filtering or LPV formulations to cope with exogenous perturbations in pitch and drivetrain loops (Kamal *et al.,* 2012; Teng *et al.,* 2021; Song *et al.,* 2022). Overall, robustness under nonlinear and time-varying regimes remains challenging, and comparative reviews underline clear trade-offs among sensitivity, modeling burden, and disturbance rejection, while synthesizing lessons from wind-energy deployments (Dey, Pisu & Ayalew, 2015; Gao & Liu, 2021; Fekih, Habibi & Simani, 2022).

To address the nonlinear, multi-regime behaviour of WTs, Takagi–Sugeno (TS) fuzzy models approximate dynamics as convex combinations of local linear models (Takagi and Sugeno, 1985; Tanaka and Wang, 2001). Building on this structure, sliding-mode observers within TS frameworks (TS-SMO) enforce suitable error dynamics and enable robust estimation for fault diagnosis (Georg and Schulte, 2013; Schulte and Gauterin, 2015). Foundational and practical aspects of sliding-mode observation are well documented in the literature (Shtessel *et al.*, 2014; Tan and Edwards, 2002), and recent WT-oriented designs report promising performance in reconstruction tasks (Borja-Jaimes *et al.*, 2022; Pérez-Pérez *et al.*, 2023).

Benchmarking and validation typically rely on the 4.8 MW wind turbine benchmark model introduced by Odgaard–Stoustrup–Kinnaert, which aggregates sensor/actuator/system faults across pitch, drivetrain, generator and converter subsystems and has become a de-facto standard for evaluating FDD/FTC strategies (Odgaard, Stoustrup & Kinnaert, 2009; Odgaard, Stoustrup & Kinnaert, 2013; Fernández-Canti *et al.,* 2015). Building on this platform, recent TS–SMO studies address rotor-torque nonlinearity by computing the torque separately and injecting it as an exogenous input, which preserves a tractable observer design and strengthens fault-reconstruction robustness (Taouil *et al.,* 2023). They further report reliable reconstruction of simultaneous sensor faults, extend the approach via an LMI-based synthesis to generator-torque and hydraulic-pitch actuator faults, and validate low estimation errors using RMSE, supporting FTC integration (Taouil, El Ougli & Tidhaf, 2024; Taouil, El Ougli & Tidhaf, 2025). Studies on WT subsystems (e.g., current-sensor faults, hydraulic pitch degradations) further emphasize the need for robust observers capable of distinguishing faults versus disturbances under varying operating conditions (Abbas, Chafouk & Ardjoun, 2024).

This paper develops a fault diagnosis scheme for the 4.8 MW benchmark based on a TS fuzzy representation of the WT and designs a Sliding-Mode Observer on this TS model to estimate actuator and sensor faults. While LMI-based SMO designs for linear/LPV systems are well established (Tan and Edwards, 2002; Alwi, Edwards & Marcos, 2012; Alwi & Edwards, 2014), the formulation is extended here to a TS framework suited to WT nonlinearities, enabling the reconstruction of generator-torque actuator faults and blade-pitch angle sensor faults under realistic wind and disturbance scenarios. All simulations are performed in MATLAB/Simulink using standard benchmark profiles.

2. Methods

2.1 Takagi–Sugeno Modeling of Wind Turbines

This study employs the 4.8 MW wind turbine benchmark model developed by Odgaard, Stoustrup, and Kinnaert (2013), which has become a widely used reference for evaluating fault diagnosis and fault-tolerant control strategies. The model integrates the main subsystems that govern wind turbine dynamics, including the aerodynamic model, the pitch actuators, the drivetrain, the generator–converter system, and a conventional proportional–integral–derivative (PID) controller, as depicted in Figure 1. This modular structure makes it possible to capture realistic operating conditions as well as the most frequent actuator and sensor fault scenarios.

The aerodynamic subsystem describes the torque produced by the rotor as a function of the blade-pitch angle β and the tip-speed ratio λ. The aerodynamic torque is expressed as:

$$\boldsymbol{\tau_r = \frac{\rho \pi R^3 C_q(\beta(t), \lambda(t)) v_w^2}{2}} \quad (1)$$

where ρ is the air density, R the rotor radius, C_q the torque coefficient depending on β and λ, and v_w the wind speed. This nonlinear relationship reflects the central role of the pitch system in regulating energy capture and protecting the turbine under high wind speeds.

Each pitch actuator, which adjusts the blade angle, is modeled by a second-order transfer function:

$$\boldsymbol{\frac{\beta_i(s)}{\beta_{re,i}} = \frac{\omega_{ni}^2}{s^2 + 2.\xi_i.\omega_{ni}.s + \omega_{ni}^2}} \quad (2)$$

where β_I denotes the actual pitch angle of blade i (i = 1, 2, 3), $\beta_{re,i}$ its reference input, ω_{ni} the natural frequency, and ξ_i the damping ratio. This model highlights the actuator's limited bandwidth and its transient behavior, which are critical in both load mitigation and fault analysis, since actuator degradations directly affect aerodynamic performance.

The drivetrain subsystem captures the mechanical coupling between the rotor and generator through the gearbox. Its dynamics are expressed in state-space form as

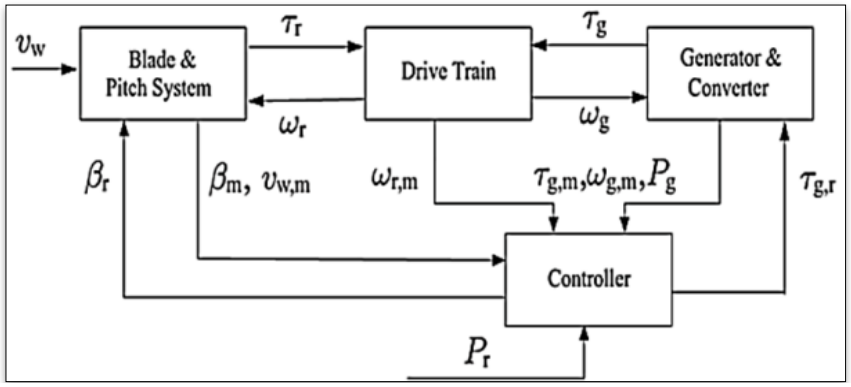

Fig. 1 General Layout of the Wind Turbine Model

$$\begin{cases} J_g.\dot{\omega}_g = -\left(\frac{\eta_{dt}B_{dt}}{N_g^2}+B_g\right)\omega_g + \frac{\eta_{dt}B_{dt}}{N_g}\omega_r + \frac{\eta_{dt}K_{dt}}{N_g}\theta - \tau_g & (3) \\ J_r\dot{\omega}_r = \frac{B_{dt}}{N_g}\omega_g - (B_{dt}+B_r)\omega_r - K_{dt}\theta + \tau_r & (4) \\ \dot{\theta} = \omega_r - \frac{1}{N_g}\omega_g & (5) \end{cases}$$

where θ is the torsional angle, ω_r and ω_g the rotor and generator angular speeds, K_{dt} and B_{dt} the drivetrain stiffness and damping, J_r and J_g the rotor and generator inertias, τ_g the generator torque, N_g the gearbox ratio, and η_{dt} the drivetrain efficiency. This representation reflects how elastic coupling and mechanical damping influence both transient and steady-state energy transfer, and it allows for fault scenarios such as gearbox wear or shaft torsion anomalies.

The generator and power converter are described with a first-order lag dynamic:

$$\frac{\tau_g}{\tau_{gre}} = \frac{1}{1+{}^{1}/_{\alpha_{gc}}s} \quad (6)$$

where τ_{gre} is the generator torque reference and α_{gc} a time constant representing converter dynamic.

The electrical power supplied by the generator is:

$$\mathrm{P_g} = \eta_g.\tau_g.\omega_g \quad (7)$$

With η_g the generator efficiency.

A PID controller is employed to track a prescribed power reference, and all constant parameter values used in these equations are taken from Odgaard, Stoustrup & Kinnaert (2013). The overall wind turbine model is thus represented in state-space form as:

$$\begin{cases} \dot{x}(t) = Ax(t) + Bu(t) & (8) \\ y(t) = Cx(t) & (9) \end{cases}$$

Where $x = [\omega_r \quad \omega_g \quad \theta \quad \dot{\beta} \quad \beta \quad \tau_g]^T$ is state vector, $u = [\tau_{gre} \quad \beta_{re}]^T$ is control input vector,

$$B = \begin{bmatrix} 0 & 0 & 0 & 0 & 0 & \alpha_{gc} \\ 0 & 0 & 0 & \omega_n^2 & 0 & 0 \end{bmatrix}^T,\ C = \begin{bmatrix} 1 & 0 & 0 & 0 & 0 & 0 \\ 0 & 1 & 0 & 0 & 0 & 0 \\ 0 & 0 & 0 & 0 & 1 & 0 \\ 0 & 0 & 0 & 0 & 0 & 1 \end{bmatrix}$$

$$A = \begin{bmatrix} a_{11} & \frac{B_{dt}}{N_g J_r} & -\frac{K_{dt}}{J_r} & 0 & 0 & 0 \\ \frac{\eta_{dt}B_{dt}}{N_g J_g} & -\frac{\frac{\eta_{dt}B_{dt}}{N_g^2}+B_g}{J_g} & \frac{\eta_{dt}K_{dt}}{N_g J_g} & 0 & 0 & -\frac{1}{J_g} \\ 1 & -\frac{1}{N_g} & 0 & 0 & 0 & 0 \\ 0 & 0 & 0 & -2\xi\omega_n & -\omega_n^2 & 0 \\ 0 & 0 & 0 & 1 & 0 & 0 \\ 0 & 0 & 0 & 0 & 0 & -\alpha_{gc} \end{bmatrix}$$

where $\boldsymbol{a_{11}} = \frac{\rho\pi R^5 C_q(\beta(t),\lambda(t))\,\omega_r}{2J_r\lambda^2} - \frac{B_{dt}+B_r}{J_r}$

Takagi–Sugeno (TS) modeling provides a rigorous yet practical way to approximate the strongly nonlinear, multi-regime dynamics of wind turbines by expressing the plant as a convex interpolation of local linear submodels scheduled by measurable premise variables (Takagi & Sugeno, 1985; Tanaka & Wang, 2001). In wind-energy applications, two well-established construction routes are used. First, sector-nonlinearity (SNL)–based polytopic embedding bounds dominant nonlinearities (such as the aerodynamic torque dependence on tip-speed ratio and pitch β) to obtain an exact or tight polytopic description over prescribed operating intervals, which is well suited to Linear Matrix Inequality (LMI)–based analysis and synthesis (Takagi & Sugeno, 1985; Tanaka & Wang, 2001; Rotondo *et al.,* 2015). Second, local linearization/identification builds submodels at representative operating points and blends them by smooth membership functions; this approach underpins designs with Parallel Distributed Compensation (PDC) (i.e., a controller/observer structure matched rule-by-rule to the TS submodels) and Model Predictive Control (MPC) formulated on TS models for region transitions and actuator constraints (Bououden *et al.,* 2012; Abdelbaky *et al.,* 2020). A complementary data-driven line leverages Adaptive Neuro-Fuzzy Inference System (ANFIS) structures to identify TS surrogates directly from input–output data for monitoring and fault diagnosis when parametric descriptions are uncertain (Pérez-Pérez et al., 2022). Across these variants, the overarching objective is to preserve the physical input–output structure —keeping B and C common whenever possible —so that vertex properties extend by convexity to the full operating envelope and a single, implementable set of observer/controller gains can be deployed; in what follows, the formulation adopted focuses on the turbine's dominant aerodynamic nonlinearity and selects a minimal, physically interpretable set of premise variables, while using the 4.8 MW benchmark as the reference dynamic description.

The main nonlinearity in the wind turbine model lies in the matrix coefficient a_{11}, which depends on the rotor angular velocity ω_r, the blade pitch angle β, and the tip-speed ratio λ, due to variations in the aerodynamic torque coefficient $C_q(\beta,\lambda)$ under different operating conditions. To approximate this nonlinear behavior, the TS fuzzy model is constructed using three premise variables: ω_r, β, and λ, each associated with specific fuzzy sets. The chosen values for these fuzzy sets are based on realistic operational limits typically encountered in a standard 4.8 MW benchmark wind turbine (Odgaard, Stoustrup & Kinnaert, 2013). Specifically, the sets are defined as follows: W_l for ω_r with l=1, 2, where $W_1 = 0.0591$ rad/s corresponds to near-idle conditions and $W_1 = 2.5$ rad/s corresponds to rated operational speed; ; $N\tau$ for β with $\tau = 1,2$, where $N_1 = -2°$ represents minimal pitch angle and $N_2 = 90°$ indicates the fully feathered position; and $V_k\ for\ \lambda$ with k=1,2,3, where $V_1 = 1, V_2 = 7, and\ V_3 = 13.$ represent low, medium, and high aerodynamic efficiency regions, respectively.

The nonlinear dynamics are approximated by 12 fuzzy rules, each corresponding to a specific combination of the premise variables $[W_l, N\tau, V_k]$ defines each rule $R_{l\tau k}$, expressed as:

If ω_r is W_l, β is N_τ , and λ is V_k, then $\begin{cases} \dot{x} = A_{l\tau k}x + B_{l\tau k}u \\ y = C_{l\tau k}x \end{cases}$

The matrix $A_{l\tau k}$ is obtained by linearizing the nonlinear element a_{11}:

$$\boldsymbol{a_{11}} = \frac{\rho\pi R^5 C_q(N\tau, Vk)\,W_l}{2J_r {V_k}^2} - \frac{B_{dt}+B_r}{J_r} \quad (10)$$

The matrices $B_{l\tau k} = B$, $C_{l\tau k} = C$ retain the original input/output structure.

To compute the activation level of each rule, membership functions are defined for each premise variable. For ω_r, two linear functions $a_1(\omega_r), a_2(\omega_r)$ are used (Fig. 2a); for β, two linear functions $b_1(\beta), b_2(\beta)$ (Fig. 2b); and for λ, three triangular functions $c_1(\lambda), c_2(\lambda), and\ c_3(\lambda)$ (Fig. 2c). The global

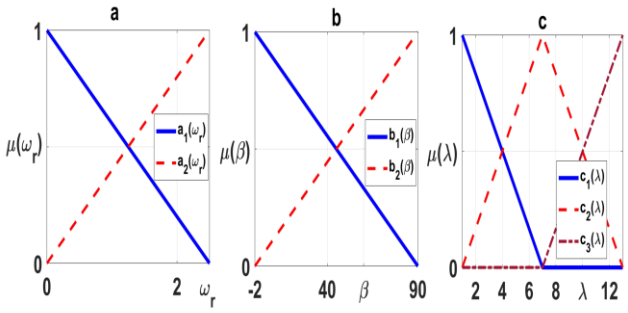

Fig. 2 Membership functions of premise variables $\omega_r, \beta, and\ \lambda$

membership functions $h_{l\tau k}(\mu) = a_l(\omega r) \cdot b_\tau(\beta) \cdot c_k(\lambda)$ combine the local submodels and satisfy the convex sum condition $\sum_{l=1}^{2}\sum_{\tau=1}^{2}\sum_{k=1}^{3} h_{l\tau k}(\mu) = 1$, with $0 \le h_{l\tau k}(\mu) \le 1$. For simplicity, the multi-index (l, τ, k) is replaced by a single index $i = 1, \dots, 12$, yielding the compact T-S fuzzy model:

$$\begin{cases} \dot{x} = \sum_{i=1}^{12} h_i(\mu)(A_i x + B_i u) & (11) \\ y = \sum_{i=1}^{12} h_i(\mu) C_i x & (12) \end{cases}$$

with $(A_i, B_i, C_i) = (A_{l\tau k}, B, C)$ according to the mapping $i \leftrightarrow (l, \tau, k)$. This construction preserves the physical input–output structure and yields a convex interpolation of local models, which is well suited to LMI-based observer synthesis and robustness analysis across the operating envelope. The vertex matrices $\{A_i\}_{i=1}^{12}$ are provided for reproducibility. The TS partition and numerical ranges follow Odgaard, Stoustrup & Kinnaert (2013). For readability, the vertex matrices $\{A_i\}_{i=1}^{12}$ and the varying entry $a_{11}^{(i)}$ are provided in Appendix A.

2.2 TS-SMO design for actuator and sensor fault estimation

The original system with actuator and sensor faults is represented as:

$$\begin{cases} \dot{x} = \sum_{i=1}^{12} h_i(\mu)(A_i x + B_i u + D_i\, f_{ac}) & (13) \\ y = \sum_{i=1}^{12} h_i(\mu)(C_i x + f_s) & (14) \end{cases}$$

Where f_{ac} and f_s denote bounded actuator and sensor faults, and $D_i = B_i = B$ for all i. A Takagi–Sugeno Sliding Mode Observer (TS-SMO) is then constructed to estimate the system states and enable the reconstruction of actuator and sensor faults. The primary objective is to ensure that the output estimation error $\varepsilon_y(t) = \hat{y}(t) - y(t)$ converges to zero in finite time, even in the presence of faults. The observer structure is:

$$\begin{cases} \dot{\hat{x}} = \sum_{i=1}^{12} h_i(\mu)\big(A_i \hat{x} + B_i u - G_{li}\varepsilon_y + G_{ni}\vartheta\big) & (15) \\ \hat{y}(\mathrm{t}) = \sum_{i=1}^{12} h_i(\mu) C_i \hat{x} & (16) \end{cases}$$

As proposed by Taouil, El Ougli & Tidhaf (2025) discontinuous switching term is weighted and normalized to enhance multi-channel robustness and to overcome the limitations of scalar-gain observers: the raw output error ε_y is first remultiplied by a diagonal normalization matrix $\mathrm{W_m} = \mathrm{diag}\big(1/\omega_{r,ave}, 1/\omega_{g,ave}, 1/\beta_{ave}, 1/\tau_{g,ave}\big)$, with $\big(\omega_{r,ave} = 1.3\,, \omega_{g,ave} = 125\ , \beta_{ave} = 2, \tau_{g,ave} = 2e^4\big)$, which scales each output component by the inverse of its typical magnitude so that the ensuing reaching dynamics are insensitive to unit/scale disparities across channels; next, a positive-definite diagonal gain $\kappa = \mathrm{diag}\big(\kappa_1, \dots, \kappa_\mathrm{p}\big)$ is used (rather than a scalar) to allocate channel-wise authority and meet per-output reaching conditions, and is set here to $\kappa = \mathrm{diag}(20,\ 200,\ 40,\ 3.5 \times 10^4)$. In this framework, the switching term is:

$$\vartheta = -\kappa \left\| P_0\, \widetilde{D}_2 \right\| \frac{W_m . \varepsilon_y}{\left\| W_m . \varepsilon_y \right\| + \delta} \qquad (17)$$

with a fixed smoothing constant δ=0.05 to avoid singularities and mitigate chattering near $W_m \varepsilon_y = 0$. Here, $\widetilde{D_2} := TM_2$ denotes the fault-distribution matrix projected onto the rotated measured subspace (obtained from the canonical/state transformation that separates fault-affected and fault-unaffected outputs), and $P_0 \succ 0$ is the weighting that shapes the injection on the measured part. The diagonal entries are selected to satisfy $\kappa_\mathrm{i} > sup_i \left|\mathrm{f_{ac,i}(t)}\right|$ (or a conservative bound thereof) so that the multi-input reaching condition holds channel by channel. Chattering is a known practical issue in sliding-mode observers, as the discontinuous injection may generate high-frequency components in the estimated signals. In this work, chattering is mitigated by introducing the boundary-layer smoothing parameter δ (here fixed to δ=0.05) in the switching function, which replaces the ideal sign operator by a continuous approximation. Increasing δ enlarges the boundary layer and therefore reduces high-frequency oscillations in the equivalent injection and in the reconstructed fault, at the expense of a slower reaching phase and a small steady tracking error; conversely, decreasing δ improves tracking accuracy but may increase high-frequency content. Similarly, the diagonal gain κ controls the reaching speed on each output channel: larger κ accelerates convergence and improves robustness to uncertainties, but it may amplify measurement noise and increase the high-frequency components of the reconstructed signal, while smaller κ yields smoother estimates but weaker disturbance rejection. In the presented simulations, the selected pair (δ, κ) provides a satisfactory compromise: the residuals remain bounded and the reconstructed signals do not exhibit drift, while no persistent high-frequency oscillations are observed in the estimation errors. From an implementation viewpoint, any remaining high-frequency content can be further attenuated by adjusting δ or by applying a low-pass filter to the reconstructed fault before feeding it to a controller, which prevents injecting switching-related components into the actuation loop. This normalized, anisotropic injection preserves the standard SMO structure while improving noise rejection and balancing the speed/robustness trade-off across outputs: W_m equalizes the effective error energy seen by the switch, κ distributes the control effort per channel, P_0 shapes the equivalent-injection dynamics later used for fault reconstruction, and δ enforces Lipschitz continuity around the origin. The observer gains $G_{li}\ and\ G_{ni}$, together with P_0 and $\widetilde{D_2}$, are then computed via the same LMI-based procedure as in Tan & Edwards (2000); this procedure is briefly described next.

To expose a fault–unaffected output subchannel (the sliding surface) common to all submodels, a single design basis is

constructed and shared. First, a coordinate change T_c is imposed so that $C\,T_c^{-1} = [\,0\ \ I_p\,]$ which yields, for each vertex i, $A_{c,i} = T_c A\,T_c^{-1} = \begin{bmatrix} A_{11i} & A_{12i} \\ A_{21i} & A_{22i} \end{bmatrix}$ and $T_c B = \begin{bmatrix} M_1 \\ M_2 \end{bmatrix}$ with $M_2 = CB$. Next, an orthogonal rotation T is selected on the measured part so that $T^T M_2 = \begin{bmatrix} 0 \\ M_0 \end{bmatrix}$ with full-rank M_0, and the block transformation $\mathrm{T_b} = \begin{bmatrix} \mathrm{I_{n-p}} & -M_1 \mathrm{M_2^{\dagger}} \\ 0 & T^T \end{bmatrix}$ is applied where $\mathrm{M_2^{\dagger}}$ denotes the (left) Moore–Penrose pseudoinverse of M_2 (assumed full column rank), i.e. $\mathrm{M_2^{\dagger}} = \left(M_2^{\top} M_2\right)^{-1} M_2^{\top}$. In the final state basis $w = T_b T_c x$, common to all vertices, one obtains $A_{a,i} = T_b A_{c,i} T_b^{-1}$, $C_a = [\,0\,T\,]$ and $M = \begin{bmatrix} 0 \\ M_0 \end{bmatrix}$ with $M_2 = \begin{bmatrix} 0 \\ M_0 \end{bmatrix}$. If the output is additionally rotated as $\tilde{y} := T\,y$, the output matrix becomes simply $C = [\,0\,I_p\,]$ in the design basis without changing $A_{a,i}$, which simplifies synthesis. The projected distribution $\widetilde{D_2} := TM_2$ remains constant (and full rank), which stabilizes subsequent reconstruction. In this design basis, the state error is defined as $e := \hat{w} - w$ (whereas $\varepsilon_y = \hat{y} - y$ mains the output error), and all stability conditions are written with $A_{a,i}$ and $C = [\,0\,I_p\,]$. Thus, the closed-loop term $(A - G_{\mathrm{l}}\,\mathrm{C})$ refers to the transformed convex combination $A_a(\mu) - G_{\mathrm{l}} C$ with $A_a(\mu) = \sum_i h_i(\mu) A_{a,i}$.

Quadratic stabilization of the observer's linear part is ensured by a Lyapunov function $\mathcal{V}(e) = e^{\top} P e$ with $P \succ 0$. Two positive-definite weighting matrices are used in the LMI synthesis: $V \succ 0$, which weights the measured-output error (noise sensitivity), and $W \succ 0$, which sets the desired convergence/robustness level. In this work, both matrices are selected diagonal for simplicity and reproducibility, namely $V = 0.2\,I_4$ and $W = 100\,I_6$. A common matrix P is then sought to satisfy, at every vertex i

$$P A_{a,i} + A_{a,i}^{\top} P - C^{\top} V^{-1} C + P W P \prec 0$$

which is implemented via the Schur complement as

$$\begin{bmatrix} P A_{a,i} + A_{a,i}^{\top} P - C^{\top} V^{-1} C & P \\ P & -W^{-1} \end{bmatrix} \prec 0$$

optionally augmented with a variable $X \geq \mathrm{P}^{-1}$ to enable convex minimization of trace(X) and tune the speed/robustness trade-off. Once a common P is available, the shared linear gain is obtained in closed form as $G_l = P^{-1} C^{\top} V^{-1}$, which guarantees that $A_a(\mu) - G_{\mathrm{l}} C$ is stabilized for every convex combination.

To embed the sliding structure and calibrate the injection explicitly, P is parameterized by blocks as $P = \begin{bmatrix} P_{11} & P_{12} \\ P_{21} & P_{22} \end{bmatrix} > 0$ with $P_{12} = [\,P_{121}\,0\,]$. Once the LMIs are solved, the surface and injection parameters are recovered as $P_1 := P_{11}, L_0 := P_{11}^{-1} P_{121}$, and $P_0 := T\left(P_{22} - \mathrm{P_{12}^{T}} P_{11}^{-1} P_{12}\right) T^{\top}$. The gain L_0 governs the reduced sliding dynamics, whereas P_0 weights the injection on the measured part and conditions the extraction of the equivalent injection. In the basis $C = [\,0\,I_p\,]$ the nonlinear gain takes the compact form $G_n = \begin{bmatrix} 0 \\ P_0^{-1} \end{bmatrix}$ (and, in the basis $C = [\,0\,T\,], G_n = \begin{bmatrix} -L \\ I_p \end{bmatrix} T^T P_0^{-1}$ with $L = [\,L_0\,0\,]$). The gains (G_{l}, G_n), together with (L_0, P_0), are common to all vertices, so that quadratic stability and surface attractivity are ensured for every μ.

Once the sliding surface is reached on the unaffected subchannel ($\varepsilon_{y_n} = 0$ and $\dot{\varepsilon}_{y_n} = 0$), the equivalent injection ϑ_{eq} is extracted and used for robust fault reconstruction. Owing to the constancy and full rank of $\widetilde{D_2}$, the sensor-fault estimate is written on the canonical partition as

$$\hat{f}_s = \sum_{i=1}^{12} h_i \left(A_{21i} A_{11i}^{-1} A_{12i} - A_{22i}\right)^{-1} P_0^{-1} \vartheta_{eq} \qquad (18)$$

The actuator-fault estimate is obtained from the projected fault distribution as

$$\hat{f}_{ac} = \widetilde{D_2}^{+} P_0^{-1} \vartheta_{eq} \qquad (19)$$

The overall design chain is thus homogeneous: the transformations T_c and T_b are applied once to obtain a common basis, the vertex LMIs are enforced with operator-chosen weights V and W, a common P is computed and yields $\mathrm{G_l}, (L_0, P_0)$ are extracted from the blocks of P, the nonlinear gain G_n is formed accordingly, the normalized/weighted switching law is implemented on the unaffected output subchannel, and the equivalent injection thereby generated enables consistent reconstruction of both actuator and sensor faults in the T–S framework. For readability, the numerical observer gains issued from the LMI solution are reported in Appendix B.

2. Results and discussion

To emulate real operating conditions, a long, highly variable wind profile (Fig. 3) was used; this input is derived from the 4.8 MW benchmark framework of Odgaard, Stoustrup & Kinnaert (2013) and is widely regarded as realistic for utility-scale turbines. Under this excitation, the TS surrogate was exercised across the main operating regions—sub-rated, transition, rated, and de-rated—and its performance was evaluated channel-by-channel against the nonlinear benchmark for rotor speed ω_r, generator speed ω_g, blade-pitch angle β, and generator torque τ_g. The accuracy of the TS model was quantified using the Normalized Sum of Squared Errors (NSSE), defined as

$$NSSE\,\% = 100 \cdot \sqrt{\frac{\sum_{i=1}^{N} (\hat{y}_i - y_i)^2}{\sum_{i=1}^{N} (y_i)^2}} \qquad (20)$$

where $\hat{y}_i$ denotes the output generated by the TS model and y_i is the corresponding output from the original nonlinear model. The resulting NSSE values for each channel are reported in Table 1.

For ω_r (upper-left panel of Fig. 4), the TS curve is practically indistinguishable from the nonlinear reference over the entire 0–4400 s horizon. The zoom around $t \approx 1750 - 1800s$ shows a slight speed dip caused by a lull and the subsequent recovery; the TS model follows both the trough and the rebound with a nearly imperceptible lag, indicating that scheduling based on $\{\omega_r, \beta, \lambda\}$ switches smoothly between local submodels without

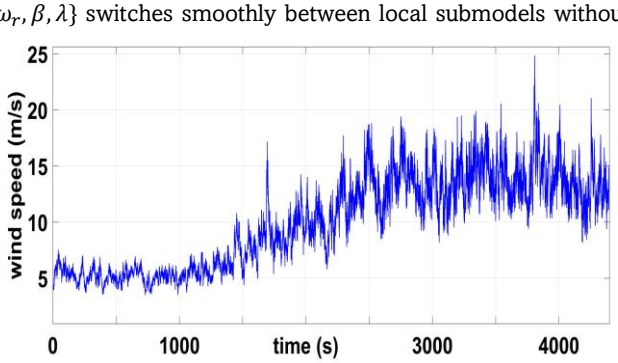

Fig. 3 Wind speed profile used as input to the system (Odgaard, Stoustrup & Kinnaert, 2013).

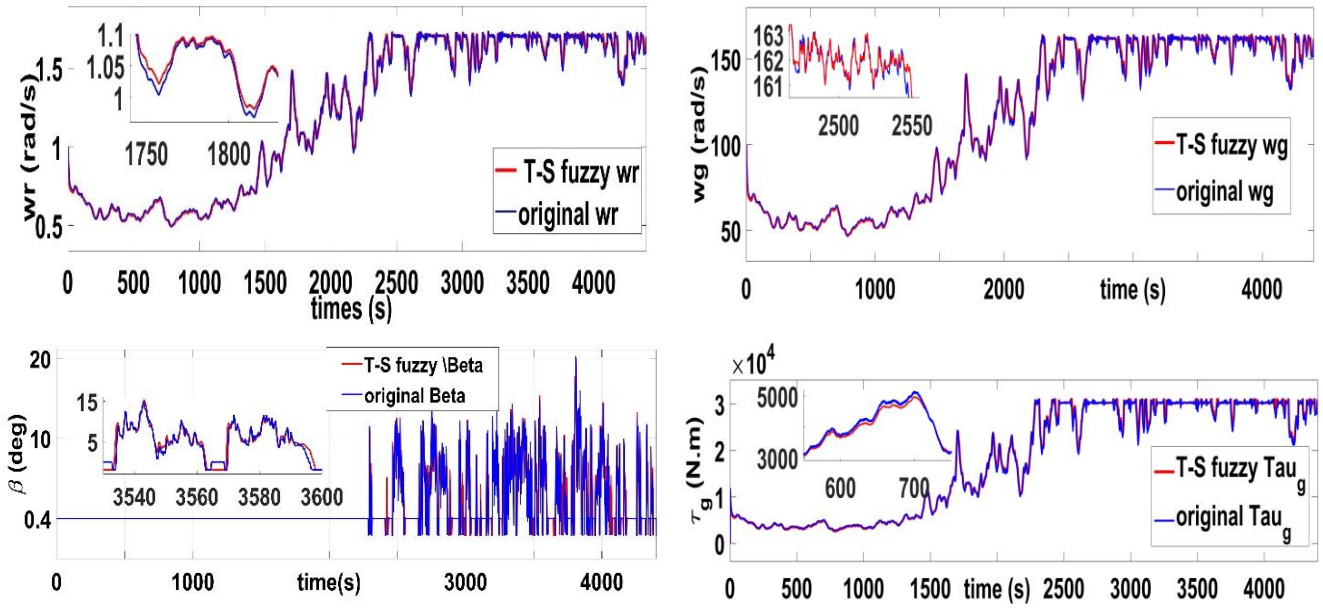

Fig. 4 Performance comparison of TS fuzzy model and nonlinear system for $\omega_r, \omega_g, \beta, and\ \tau_g$

introducing artificial phase shifts. This zoom window is presented as a representative, indicative segment of the full 0–4400 s record—illustrative rather than exhaustive—with similar behavior observed elsewhere; the same indicative-zoom convention is used for the other three figures. The resulting $NSSE = 0.86\%$ reflects this near-perfect overlap and confirms that TS interpolation preserves the dominant inertial and aerodynamic couplings shaping rotor dynamics.

A comparable conclusion holds for ω_g (upper-right). The long record shows tight tracking, including the gradual climb toward rated conditions and the many micro-transients caused by turbulence. The zoom at $t \approx 2450 - 2550s$ ($speed \sim 161 - 163rad/s$) reveals an almost imperceptible amplitude offset during very small oscillations; this behavior is typical when local linear models smooth slightly different stiffness/damping levels across neighboring rules. The offset is short-lived and bounded, and the overall error remains low with $NSSE = 0.85\%$. Together with the ω_r result, this indicates that drivetrain elasticity and gearbox scaling embedded in the reference model are properly represented by the convex blend of vertex models.

For the generator torque τ_g (lower-right), the agreement remains excellent except during fast set-point ramps. The zoom around $t \approx 600 - 700s$ shows a small amplitude discrepancy at the top of a plateau—consistent with the first-order converter dynamics, with the fact that TS rules "average" local behavior during rapid scheduler moves, and with torque limiting/saturation effects that are difficult to reproduce exactly with a modest number of rules. These localized excursions raise the error slightly but the global fit stays tight, yielding $NSSE =$ 1.72%, which is fully compatible with observer design and with fault-tolerant control requirements.

Table 1
NSSE-Based Evaluation of TS Model Accuracy Against the Original Nonlinear Wind Turbine Model

TS model / original	NSSE
Rotor speed ω_r	0.86%
Generator speed ω_g	0.85%
Pitch angle β	8.8%
generator torque τ_g	1.72%

The pitch angle β (lower-left) is the most challenging signal. The TS and nonlinear curves coincide well during slow adjustments (for instance before 2200 s), whereas larger deviations appear when the pitch system operates near constraints (rate and position limits) or alternates between low activity and active feathering. After 2200 s, the nonlinear reference exhibits rapid fluctuations due to controller activity under turbulent gusts and pitch-rate saturation, while the TS response is noticeably smoother; this smoothing reflects both the second-order actuator model and the convex interpolation, which cannot reproduce arbitrarily abrupt changes unless a denser rule base is used in these regimes. The $NSSE = 8.8\%$ is therefore concentrated in short windows of intense pitch activity; outside these windows, tracking remains accurate and unbiased. Two targeted refinements would reduce this residual if needed: augmenting the local models with a pitch-rate state to capture actuator dynamics more explicitly, and enriching the rule base near the rated/feathering neighborhood to better resolve fast β transitions.

From a system perspective, three observations emerge. First, the TS surrogate preserves the energy-carrying channels with high fidelity: ω_r, ω_g, and τ_g all exhibit NSSE values below 2% with no visible drift or phase lag at regime transitions. Second, the remaining gap on β is localized to short, constraint-dominated episodes and is structurally explained by actuator limits combined with relatively sparse rule coverage in that portion of the domain; importantly, it does not contaminate the slower mechanical states. Third, the scheduling behaves smoothly, with no fluttering or spurious resonance when rule dominance changes, as evidenced by the clean overlays and the short, bounded nature of the zoomed discrepancies. These findings support the TS surrogate as an accurate and computationally light representation of the nonlinear plant for long-horizon simulations. In practical terms, the low NSSEs on ω_r, ω_g, and τ_g ensure that observers and diagnostic algorithms tuned on the TS model will experience residual dynamics nearly identical to those of the nonlinear benchmark. The moderate NSSE on β can be mitigated—if pitch-loop precision becomes

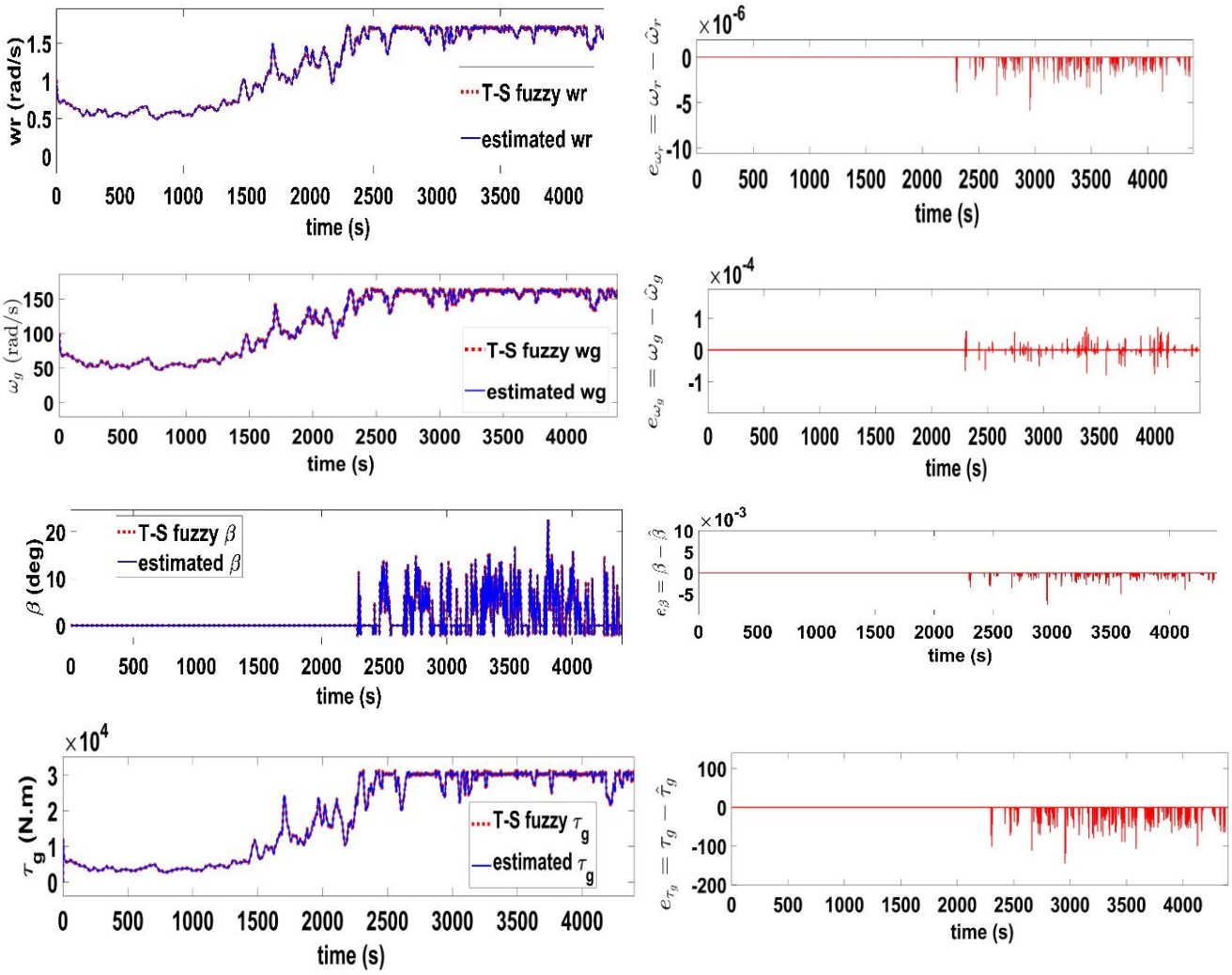

Fig. 5 Performance comparison of TS fuzzy outputs and TS-SMO estimates for $\omega_r, \omega_g, \beta, and\ \tau_g$, with estimation errors $e = y - \hat{y}$.

critical—by densifying the rules and augmenting the actuator state, without altering the rest of the pipeline. Overall, the evidence from Fig. 4 and Table 1 confirms that the proposed TS fuzzy model captures the turbine's dominant dynamics with sufficient accuracy to support real-time state observation and robust fault reconstruction while keeping the online computational load low across a wide operating range.

Figure 5 reports the full-horizon tracking performance of the proposed TS–SMO by juxtaposing the TS fuzzy outputs (reference, red dashed) with the TS–SMO estimates (blue) for $\omega_r, \omega_g, \beta, and\ \tau_g$, and by plotting the corresponding residuals $e = y - \hat{y}$ on the right-hand side. Overall, the estimated trajectories are almost indistinguishable from the TS references, which indicates that the sliding surface is reached rapidly and maintained despite operating-point changes and wind-induced variability. For the rotor speed $\omega_r,$, the overlap remains tight over the entire record, and the residual e_{ω_r} stays confined to a very small band (order of 10^{-6} in the error plot), revealing negligible bias and no drift —an important property because ω_r, reflects the dominant drivetrain energy exchange and is highly sensitive to modeling mismatches. A similar behavior is observed for the generator speed , ω_g: the estimator reproduces both the gradual evolution and the turbulence-driven micro-transients, while the residual e_{ω_g} remains close to zero with only small, bounded fluctuations (order of 10^{-4}), consistent with the fact that the TS–SMO injection compensates uncertainties on the measured subspace while the smoothing (boundary layer) prevents high-frequency chattering from corrupting the estimate. The pitch angle β is, as expected, the most "excited" channel (frequent and fast variations due to controller activity and actuator dynamics), and the residual e_β exhibits the largest excursions among the four outputs (order of 10^{-3}); however, these excursions remain bounded and do not accumulate, which is precisely the behavior desired for diagnosis: transients are visible at sharp β changes, but the estimate rapidly returns to the reference without long-lasting oscillations. Finally, the generator torque τ_g is tracked with good fidelity in amplitude and trend, while e_{τ_g} remains bounded (visible negative spikes but no divergence), indicating that the observer preserves torque dynamics even during faster variations that typically stress converter/actuator representations. Table 2 complements these time-domain observations by condensing the tracking performance into RMSE values for each channel, confirming that the estimation error energy remains extremely small and bounded for $\omega_r, \omega_g,$ and β, while the torque channel τ_g is also reconstructed with a low absolute error level relative to its operating range. For additional perspective, the same table reports representative RMSE values available in the literature for pitch/drivetrain fault-estimation observers, namely the augmented-state UIO and the H_∞ observer reported by Azizi *et*

Table 2
RMSE-Based Performance Comparison of TS-SMO with Baseline Observers for Wind Turbine Outputs

Output	RMSE (TS-SMO) (this work)	RMSE (UIO) Azizi et al.	RMSE (H∞ observer) Azizi et al.
ω_r (rad/s)	1.6×10^{-7}	–	–
ω_g (rad/s)	3.5×10^{-7}	8×10^{-4}	6×10^{-4}
β °	1.7×10^{-4}	1.5×10^{-3}	3.6×10^{-3}
τ_g (N. m)	5 .55	–	–

Note: "–" denotes not reported in Azizi et al. (2024) for the corresponding output

al. (2024), where the corresponding state channels include $x_2 = \omega_g$ *and* $x_4 = \beta$. In that reference, RMSE values on the order of 10^{-4} for ω_g and 10^{-3} for β are reported, providing a quantitative baseline for these two variables.

When juxtaposed with the results obtained here, the markedly smaller RMSE levels achieved by the TS–SMO on ω_g, and β indicate a strong tracking capability of the proposed design, consistent with the tight superposition observed in Figure **5** and the bounded residuals $e = y - \hat{y}$. This quantitative framing is particularly relevant because RMSE is widely adopted as a primary performance index to assess fault/state reconstruction quality in robust observer-based designs for wind-turbine pitch and drivetrain subsystems. These results naturally motivate the subsequent discussion on the generator-torque channel, which is well known to be a critical and fault-prone actuation pathway in modern wind-turbine system

The generator torque input in wind turbine systems is particularly susceptible to actuator faults such as biased output, low or high output, random fluctuations, and delayed actuation. These anomalies typically arise from failures in the power converter, converter controller, or associated sensors, leading to incorrect torque commands, power offsets, or undesirable dynamic behavior. As a result, such faults can reduce power production efficiency and even compromise system stability.

Similarly, faults affecting the pitch system (such as bias, fixed or random output, signal loss, or slower actuation) can originate from the pitch actuator, controller, or sensor. These faults often result in inaccurate pitch angle measurements or actuation, which degrade aerodynamic control, increase structural loads, and accelerate component fatigue.

Figure 6 examines an actuator-fault scenario in which a piecewise-constant offset $f_{ac}(t)$ is injected on the generator-torque channel while the turbine is driven by the realistic wind record of Fig. 3. The true fault (solid blue) begins at $t \approx 800\ s$, undergoes several level changes—including a sign inversion—and vanishes near $t \approx 1600\ s$. The TS-SMO estimate $\hat{f}_{ac}$ (dotted red) recovers the plateaus with virtually no steady-state bias and only tiny, short-lived transients at step onsets/offsets. The inset around the first plateau shows a bounded peak on the order of 5×10^{-2} relative to a $\sim 1.5 \times 10^{3}$ amplitude, i.e., a negligible $< 0.01\%$ overshoot. This behavior is consistent with the equivalent-injection mechanism: when the sliding surface is reached, the discontinuous law and the normalization W_m drive the output error to zero rapidly; the small peaks are shaped by the diagonal gain κ and the smoothing constant δ, which temper chattering without introducing noticeable delay. The circled region around the highest positive plateau illustrates that the estimate remains well aligned even after multiple scheduler moves, indicating that the projected fault-distribution matrix $\widetilde{D_2}$ is well conditioned in the adopted canonical/output basis and that the pseudoinverse $\widetilde{D_2}^{+}$ does not amplify noise. Quantitatively, the actuator-fault NSSE is 7.68%. This value is dominated by the very brief edges at each step (exactly the segments most penalized by an energy-based metric) whereas the intervals that matter for fault-tolerant control (constant-bias plateaus used for compensation) are matched almost exactly in sign and magnitude.

Figure 7 considers a sensor-fault case f_s modeled as a bias on the pitch-angle measurement, active approximately on $t \in [2000,2700]$ s. The reconstruction $\hat{f}_s$ tracks the reference nearly point-for-point: the rise and fall times are close to the true transitions, the plateau level is recovered without noticeable offset, and the only visible deviations are narrow spikes at the beginning of the bias (see the inset around 2200–2400 s). These spikes are bounded reaching transients of the equivalent injection under turbulent excitation and are intentionally attenuated by W_m and δ. The resulting sensor-fault NSSE is extremely low, 0.087%, which reflects two design features: (i) in the canonical/output basis the sliding surface is imposed on an output subchannel unaffected by actuator inputs, so the sensor bias is conveyed directly in the equivalent injection; and (ii) no inversion of $\widetilde{D_2}$ is required, further improving robustness to modeling error and measurement noise.

Taken together, the two experiments show that the TS-SMO achieves fast reaching, negligible plateau bias, and bounded, non-oscillatory transients for both actuator and sensor faults under realistic, time-varying conditions. The higher NSSE observed for the actuator case is explained by its intermittent,

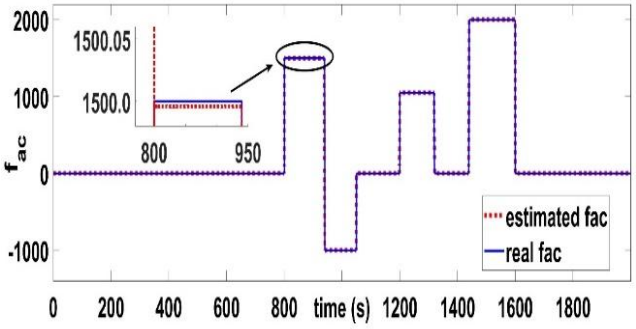

Fig. 6 Real actuator fault f_{ac} and its estimated $\hat{f}_{ac}$.

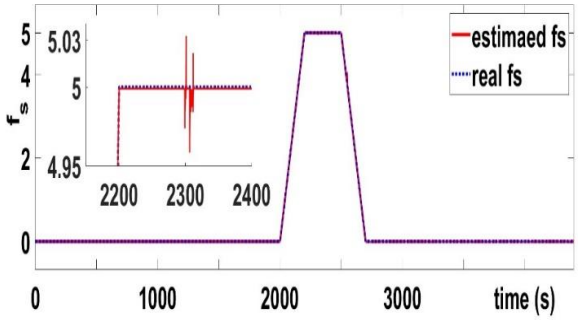

Fig. 7 Real sensor fault $\mathbf{f_s}$ and its estimated $\hat{\mathbf{f}}_\mathbf{s}$

multi-step nature rather than by systematic estimation error; by contrast, the measurement-path bias is recovered almost ideally. From a control perspective, these properties satisfy the core requirements for fault-tolerant operation: detection is timely, the reconstructed magnitudes are accurate enough for compensation without destabilizing the torque or pitch loops, and the residual noise is small. If even tighter performance were required, two low-risk refinements are available: slightly increasing κ (or reducing δ) on the affected channel to further limit edge peaking, and enriching the TS rule base in operating zones where very sharp transitions are frequent.

Taken together with the NSSE results above, these reconstructions clarify how a physics-based TS–SMO differs from common SCADA-driven machine-learning approaches. Machine-learning models (e.g., deep autoencoders, CNN/LSTM hybrids, and tree ensembles) can flag subtle anomalies early when large, representative datasets are available; however, they often require labeled faults (or carefully designed proxy labels), periodic retraining to accommodate operating-point drift, and post hoc explainability to link anomaly scores to physical root causes (Tautz-Weinert & Watson, 2017; Zhao *et al.*, 2018; Maldonado-Correa *et al.*, 2020; Pandit et al., 2022). In contrast, the proposed TS–SMO embeds plant physics through a Takagi–Sugeno fuzzy decomposition with sliding-mode injection, which preserves interpretability because residuals and estimates map directly to states and inputs, provides formal robustness with fast error convergence under bounded uncertainties, and reconstructs both the magnitude and the sign of faults, thereby yielding actionable information for fault-tolerant control (FTC) rather than a unitless anomaly index (Tan & Edwards, 2002; Alwi & Edwards, 2014; Shtessel *et al.,* 2014). The associated online computational burden is modest, consisting primarily of matrix updates with a bounded discontinuous term, which facilitates real-time deployment on industrial controllers.

4. Conclusions and outlook

This study presented a TS-fuzzy modeling and Sliding-Mode Observer (SMO) scheme for fault diagnosis on the 4.8 MW benchmark. The TS model captures multi-regime nonlinearities while enabling LMI-based observer synthesis, and the SMO achieves fast, robust reconstruction of generator-torque actuator faults and blade-pitch sensor faults, with reduced sensitivity to gain scaling and disturbances compared with baseline robust observer frameworks reported in the literature. The weighted/normalized switching structure ($\boldsymbol{W_m}$, diagonal $\boldsymbol{\kappa}$, and boundary-layer smoothing δ) offers a practical accuracy–robustness compromise by reducing gain-scaling effects across channels and limiting chattering-related high-frequency components, while keeping the online computations lightweight (matrix operations plus a bounded switching term). The method is readily integrable into existing monitoring/control stacks. Main caveats are the dependence on an adequate TS partition and the need to mitigate SMO chattering; large parameter drifts beyond the TS envelope may require retuning or rule-base enrichment. Building on these results, future work will focus on embedding the estimator within a closed-loop FTC scheme for real-time reconfiguration, extending the design toward incipient-fault detection and prognosis via adaptive gain scheduling, validating on hardware-in-the-loop/test-bench while quantifying delays, quantization, and dropouts, and benchmarking under turbulent/gusty winds, grid events, and offshore scenarios.

References

Abbas, M., Chafouk, H., & Ardjoun, S.A.E.M. (2024). Fault diagnosis in wind turbine current sensors: Detecting single and multiple faults with the extended Kalman filter bank approach. *Sensors*, 24(3), 728; https://doi.org/10.3390/s24030728

Abdelbaky, M.A., Liu, X., & Jiang, D. (2020). Design and implementation of partial offline fuzzy model-predictive pitch controller for large-scale wind-turbines. *Renewable Energy*, 145, 981–996; https://doi.org/10.1016/j.renene.2019.05.074

Alwi, H., Edwards, C., & Tan, C.P. (2011). Fault Detection and Fault-Tolerant Control Using Sliding Modes. *Springer*; https://doi.org/10.1007/978-1-4471-2161-3

Alwi, H., Edwards, C., & Marcos, A. (2012). Fault reconstruction using a LPV sliding mode observer for a class of LPV systems. *Journal of the Franklin Institute*, 349(2), 510–530; https://doi.org/10.1016/j.jfranklin.2011.06.026

Alwi, H., & Edwards, C. (2014). Robust fault reconstruction for linear parameter varying systems using sliding mode observers. *International Journal of Robust and Nonlinear Control*, 24(14), 1947–1968; https://doi.org/10.1002/rnc.3018

Apkarian, P., Gahinet, P., & Becker, G. (1995). Self-scheduled H∞ control of linear parameter-varying systems: A design example. *Automatica*, 31(9), 1251–1261; https://doi.org/10.1016/0005-1098(95)00038-X

Azizi, A., Youssef, T., Kouadri, A., Mansouri, M., & Mimouni, M. F. (2024). Robust fault estimation for wind turbine pitch and drive train systems. International Journal of Electrical Power & Energy Systems, 155(Part B), 109673; https://doi.org/10.1016/j.ijepes.2023.109673

Borja-Jaimes, V., Adam-Medina, M., López-Zapata, B.Y., Vela Valdés, L.G., Claudio Pachecano, L., & Sánchez Coronado, E.M. (2022). Sliding mode observer-based fault detection and isolation approach for a wind turbine benchmark. *Processes*, 10(1), 54; https://doi.org/10.3390/pr10010054

Bououden, S., Chadli, M., Filali, S., & El Hajjaji, A. (2012). Fuzzy model based multivariable predictive control of a variable speed wind turbine: LMI approach. *Renewable Energy*, 37(1), 434–439; https://doi.org/10.1016/j.renene.2011.06.025

Boyd, S., El Ghaoui, L., Feron, E., & Balakrishnan, V. (1994). Linear Matrix Inequalities in System and Control Theory. *SIAM*; https://doi.org/10.1137/1.9781611970777

Cao, M., Chen, X., & Jiang, D. (2016). Wind turbine fault diagnosis based on unscented Kalman filter and SCADA data. *Energies*, 9(10), 847; https://doi.org/10.3390/en9100847

Chen, J., & Patton, R.J. (1999). Robust Model-Based Fault Diagnosis for Dynamic Systems. *Kluwer/Springer*; https://doi.org/10.1007/978-1-4615-5149-2

Dey, S., Pisu, P., & Ayalew, B. (2015). A comparative study of three fault diagnosis schemes for wind turbines. *IEEE Transactions on Control Systems Technology*, 23(5), 1853–1868; https://doi.org/10.1109/TCST.2015.2389713

Efimov, D., Raïssi, T., Zolghadri, A., & Perruquetti, W. (2016). Design of interval observers for uncertain dynamical systems. *Automation and Remote Control,* 77(2), 191–225; https://doi.org/10.1134/S0005117916020016

Fekih, A., Habibi, H., & Simani, S. (2022). Fault diagnosis and fault tolerant control of wind turbines: An overview. *Energies*, 15(19), 7186; https://doi.org/10.3390/en15197186

Fernandez-Canti, R.M., Blesa, J., Tornil-Sin, S., & Puig, V. (2015). Fault detection and isolation for a wind turbine benchmark using a mixed Bayesian/set-membership approach. *Annual Reviews in Control*, 40, 59–69; https://doi.org/10.1016/j.arcontrol.2015.08.002

Gao, Z., & Liu, X. (2021). An overview on fault diagnosis, prognosis and resilient control for wind turbine systems. *Processes*, 9(2), 300; https://doi.org/10.3390/pr9020300

Georg, S., & Schulte, H. (2013). Actuator fault diagnosis and fault-tolerant control of wind turbines using a Takagi–Sugeno sliding mode observer. In 2013 Conference on Control and Fault-Tolerant Systems (SysTol) (pp. 516–522). *IEEE*; https://doi.org/10.1109/SysTol.2013.6693872

GWEC. (2025). Global Wind Report 2025. Global Wind Energy Council.

Kamal, E., Aitouche, A., Ghorbani, R., & Bayart, M. (2012). Unknown Input Observer with Fuzzy Fault Tolerant Control for Wind Energy System. *IFAC Proceedings Volumes*, 45(20), 946–951; https://doi.org/10.3182/20120829-3-MX-2028.00069

Maldonado-Correa, J., Martín-Martínez, S., Artigao, E., & Gómez-Lázaro, E. (2020). Using SCADA data for wind turbine condition monitoring: A systematic literature review. *Energies*, 13(12), 3132; https://doi.org/10.3390/en13123132

Mazenc, F., & Bernard, O. (2011). Interval observers for linear time-invariant systems with disturbances. *Automatica*, 47(1), 140–147; https://doi.org/10.1016/j.automatica.2010.10.019

Odgaard, P.F., Stoustrup, J., & Kinnaert, M. (2009). Fault tolerant control of wind turbines – A benchmark model. *IFAC Proceedings Volumes,* 42(8), 155–160; https://doi.org/10.3182/20090630-4-ES-2003.00026

Odgaard, P.F., Stoustrup, J., & Kinnaert, M. (2013). Fault-tolerant control of wind turbines: A benchmark model. *IEEE Transactions on Control Systems Technology,* 21(4), 1168–1182; https://doi.org/10.1109/TCST.2013.2259235

Pandit, R., Astolfi, D., Hong, J., Infield, D., & Santos, M. (2023). SCADA data for wind turbine data-driven condition/performance monitoring: A review on state-of-art, challenges and future trends. *Wind Engineering*, 47(2), 422–441; https://doi.org/10.1177/0309524X221124031

Pérez-Pérez, E.J., López-Estrada, F.R., Puig, V., Valencia-Palomo, G., & Santos-Ruiz, I. (2022). Fault diagnosis in wind turbines based on ANFIS and Takagi–Sugeno interval observers. *Expert Systems with Applications,* 206, 117698; https://doi.org/10.1016/j.eswa.2022.117698

Rotondo, D., Puig, V., Nejjari, F., & Witczak, M. (2015). Automated generation and comparison of Takagi–Sugeno and polytopic quasi-LPV models. *Fuzzy Sets and Systems*, 277, 44–64; https://doi.org/10.1016/j.fss.2015.02.002

Schulte, H., & Gauterin, E. (2015). Fault-tolerant control of wind turbines with hydrostatic transmission using Takagi–Sugeno and sliding mode techniques. *Annual Reviews in Control*, 40, 82–92; https://doi.org/10.1016/j.arcontrol.2015.08.003

Shtessel, Y., Edwards, C., Fridman, L., & Levant, A. (2014). Sliding Mode Control and Observation. *Birkhäuser;* https://doi.org/10.1007/978-0-8176-4893-0

Song, Y., Jeon, T., Paek, I., & Dugarjav, B. (2022). Design and validation of pitch H-infinity controller for a large wind turbine. *Energies*, 15(22), 8763; https://doi.org/10.3390/en15228763

Tan, C.P., & Edwards, C. (2000). An LMI approach for designing sliding mode observers. *In Proceedings of the 39th IEEE Conference on Decision and Control (CDC),* 2587–2592; https://doi.org/10.1080/00207170110081723

Tan, C.P., & Edwards, C. (2002). Sliding mode observers for detection and reconstruction of sensor faults. *Automatica*, 38(10), 1815–1821; https://doi.org/10.1016/S0005-1098(02)00098-5

Tanaka, K., & Wang, H.O. (2004). Fuzzy Control Systems Design and Analysis: A Linear Matrix Inequality Approach. John Wiley & Sons.

Taouil, M., El Ougli, A., Tidhaf, B., & Zrouri, H. (2023). Sensor fault reconstruction for wind turbine benchmark model using a modified sliding mode observer. *International Journal of Electrical & Computer Engineering*, 13(5), 5066–5075; http://doi.org/10.11591/ijece.v13i5.pp5066-5075

Taouil, M., Tidhaf, B., & El Ougli, A. (2024). Actuator fault estimation in wind turbine using a modified sliding mode observer based on Linear Matrix Inequality approach. *Diagnostyka,* 25(2), 1–9; https://doi.org/10.29354/diag/187887

Taouil, M., El Ougli, A., & Tidhaf, B. (2025). Fault reconstruction of wind turbine actuators based on a modified sliding mode observer and evaluation of its accuracy using the root mean square error criterion. *Interactions,* 246(1), 42; https://doi.org/10.1007/s10751-025-02261-4

Tautz-Weinert, J., & Watson, S.J. (2017). Using SCADA data for wind turbine condition monitoring—A review. *IET Renewable Power Generation,* 11(4), 382–394; https://doi.org/10.1049/iet-rpg.2016.0248

Teng, J., Li, C., Feng, Y., Yang, T., Zhou, R., & Sheng, Q.Z. (2021). Adaptive observer-based fault-tolerant control for sensor and actuator faults in wind turbines. *Sensors*, 21(24), 8170; https://doi.org/10.3390/s21248170

Wu, P., Liu, Y., Ferrari, R.M.G., & van Wingerden, J.-W. (2021). Floating offshore wind turbine fault diagnosis via regularized dynamic canonical correlation and Fisher discriminant analysis. *IET Renewable Power Generation,* 15(16), 4006–4018; https://doi.org/10.1049/rpg2.12319

WWEA. (2025). Global Wind Power Statistics 2024/2025. World Wind Energy Association.

Zhang, Y., Lv, Y., & Ge, M. (2021). Time–frequency analysis via complementary ensemble adaptive local iterative filtering and enhanced maximum correlation kurtosis deconvolution for wind turbine fault diagnosis. *Energy Reports*, 7, 2418–2435; https://doi.org/10.1016/j.egyr.2021.04.045

Zhao, H., Liu, H., Hu, W., & Yan, X. (2018). Anomaly detection and fault analysis of wind turbine components based on deep learning network. Renewable *Energy,* 127, 825–834; https://doi.org/10.1016/j.renene.2018.05.024

Appendix A. TS benchmark matrices A_i

$$A_i = \begin{bmatrix} a_{11}^{(i)} & 1.4842\text{e}^{-7} & -4.9091\text{e}^{1} & 0 & 0 & 0 \\ 2.0303\text{e}^{-2} & -1.1714\text{e}^{-1} & 7.0688\text{e}^{4} & 0 & 0 & -2.5641\text{e}^{-3} \\ 1 & -1.0526\text{e}^{-2} & 0 & 0 & 0 & 0 \\ 0 & 0 & 0 & -1.3332\text{e}^{1} & -1.2343\text{e}^{2} & 0 \\ 0 & 0 & 0 & 1 & 0 & 0 \\ 0 & 0 & 0 & 0 & 0 & -50 \end{bmatrix}$$

with $a_{11}^{(i)}$ given as follows:

$a_{11}^{(1)} = 0.0051$	$a_{11}^{(2)} = 0.2144$	$a_{11}^{(3)} = -1.2328e^{-6}$	$a_{11}^{(4)} = 5.3553\text{e}^{-4}$
$a_{11}^{(5)} = 0.0016$	$a_{11}^{(6)} = 0.0697$	$a_{11}^{(7)} = -0.0099$	$a_{11}^{(8)} = -0.4181$
$a_{11}^{(9)} = -7.4479\text{e}^{-4}$	$a_{11}^{(10)} = -0.0309$	$a_{11}^{(11)} = -0.0124$	$a_{11}^{(12)} = -0.0124$

Appendix B. LMI solution matrices and observer gains

$$P = \begin{bmatrix} 7.4010 & 0 & -0.0033 & 0 & 0.0659 & -0.000 \\ 0 & 0.0134 & 0 & -0.0376 & 0 & 0 \\ -0.0033 & 0 & 0.1574 & 0 & -0.0001 & 0.0000 \\ 0 & -0.0376 & 0 & 0.3095 & 0 & 0 \\ 0.0659 & 0 & -0.0001 & 0 & 0.0021 & -0.000 \\ -0.0000 & 0 & 0.0000 & 0 & -0.0000 & 0.7708 \end{bmatrix}, P_0 = \begin{bmatrix} 0.1574 & 0 & -0.0001 & 0.0000 \\ 0 & 0.3095 & 0 & 0 \\ -0.0001 & 0 & 0.0021 & -0.0000 \\ 0.0000 & 0 & -0.0000 & 0.7708 \end{bmatrix}, L_0 = \begin{bmatrix} -0.0004 & 0 \\ 0 & -2.8004 \end{bmatrix}$$

$$G_n = \begin{bmatrix} 6.3527 & -0.1911 & 0 & -0.0000 \\ -0.1911 & 472.8854 & 0 & -0.0000 \\ 0.0028 & -0.0001 & 0 & -0.0000 \\ 0 & 0 & -13.7107 & 0 \\ 0 & 0 & 4.8960 & 0 \\ -0.0000 & -0.0000 & 0 & 1.2974 \end{bmatrix},$$

$$G_l = \begin{bmatrix} 31.7632 & -0.7154 & 0 & -0.0000 \\ -0.7154 & 3271.6908 & 0 & -0.0000 \\ 0.0770 & 29.1226 & 0 & 0.0000 \\ 0 & 0 & 68.5536 & 0 \\ 0 & 0 & 24.4799 & 0 \\ -0.0000 & -0.0000 & 0 & 6.4869 \end{bmatrix},$$

$$\widetilde{D_2} = \begin{bmatrix} 0 & 0 \\ 0 & 0 \\ 0 & 0 \\ 50 & 0 \end{bmatrix}$$